

Direct calculation with a finite-element method of the Laplace transform of the distribution of photon time of flight in tissue

Martin Schweiger and Simon R. Arridge

Reconstruction methods for optical tomographic imaging require the development of models of light transport in highly scattering materials. While the simulation of the full temporal response function arising from a short source light pulse is computationally expensive, there are methods to evaluate efficiently certain transforms of the temporal profile. We previously presented methods to obtain directly the Mellin transform, which is related to the moments of the temporal intensity distribution; We introduce a similar method to calculate directly the Laplace transform. This method provides an additional, largely independent measurement type that can be combined with the moments to improve image quality in optical tomography, in particular with respect to the simultaneous reconstruction of absorption and scattering distributions. © 1997 Optical Society of America

Key words: Diffusion equation, Laplace transform, temporal filtering, finite-element method.

1. Introduction

Time-resolved optical tomography is a medical imaging modality used to determine the spatially resolved absorption and scattering coefficients of light in tissue. Applications include breast imaging,¹ localized monitoring of cerebral oxygenation in infants during and after birth,^{2,3} functional brain activation during mental or physical tasks,⁴ and oxygen consumption in muscle.⁵ Data acquisition systems for optical tomography can be divided into cw-systems, which measure the intensity transmitted from a cw source; frequency-domain systems, which use intensity-modulated light sources and measure the phase shift and modulation amplitude of the transmitted signal; and time-of-flight systems, which probe the tissue with ultrashort light pulses and measure the temporal distribution of the transmitted radiation [exitance, $\Gamma(t)$] with detectors of high temporal resolution. Reconstruction algorithms for all three

types of system are currently being developed.⁶⁻¹² We concentrate on aspects of reconstruction for the time-domain case.

For imaging applications it is not normally necessary to use the full temporal measurement signal because the characteristic general shape of the function does not vary significantly with the optical properties of the probed medium and does not include high-frequency features. Instead, one seeks to derive a set of statistics that fully describe the temporal distribution. These statistics form the data vector used in the reconstruction procedure.

The choice of the optimal data type that reconstructs simultaneously both absorption and scatter is still an open question.¹³ Previously we proposed the Mellin transform as a way to extract the temporal moments of $\Gamma(t)$ and demonstrated a method to do this in a computationally efficient way using a finite-element-based forward solver.¹⁴ The use of temporal moments has the additional advantage of being intrinsically normalized, which eliminates calibration problems of the data acquisition system such as source power and detector sensitivity fluctuations or coupling efficiency changes.

We previously presented reconstructions from multiple temporal moments and from a combination of moments and the integrated intensity.¹⁵ However, the use of multiple moments suffers from the strong correlation between them and, while the combination of integrated intensity and a moment yields good re-

M. Schweiger is with Department of Medical Physics and Bio-engineering, University College London, Capper Street, London WC1E 6JA, England. S. R. Arridge is with Department of Computer Science, University College London, Gower Street, London WC1E 6BT, England.

Received 17 December 1996; revised manuscript received 27 May 1997.

0003-6935/97/349042-08\$10.00/0

© 1997 Optical Society of America

sults for simulated data, the problems in acquiring unnormalized data types mentioned above limit its use in practice.

We propose the use of the normalized Laplace transform of $\Gamma(t)$ as an additional measurement to provide a complementary type to the Mellin transform. In the following sections we discuss methods for generating the forward signal and its derivative for this data type. These are the essential elements required for any new measurement type to be incorporated into our reconstruction algorithm.

2. Light Transport Model

We describe the propagation of light within a region of tissue in terms of the spatial and the temporal distribution of the photon density, $\Phi(\mathbf{r}, t)$. Numerous studies show that for the range of optical parameters encountered in biological tissues the diffusion equation is an adequate model for Φ ¹⁶⁻¹⁹:

$$\frac{1}{c} \frac{\partial \Phi(\mathbf{r}, t)}{\partial t} - \nabla \cdot \kappa(\mathbf{r}) \nabla \Phi(\mathbf{r}, t) + \mu_a(\mathbf{r}) \Phi(\mathbf{r}, t) = q_0(\mathbf{r}, t), \quad (1)$$

inside a domain Ω , bounded by $\partial\Omega$, where $\kappa(\mathbf{r}) = [3(\mu_a + \mu_s')]^{-1}$ is the diffusion coefficient, $\mu_s' = (1 - f)\mu_s$ is the reduced scattering coefficient, μ_a and μ_s are the absorption and scattering coefficients, respectively, f is an anisotropy factor given by the mean cosine of a single scattering event, and c is the speed of light in the medium.

The diffusion equation is valid in scatter-dominated media ($\mu_s' \gg \mu_a$) at sufficiently large distances between source and detector ($\gg 1/\mu_s'$). The former condition is generally true in the near-infrared wavelength band for all biological tissue types considered here, and the latter condition can be ensured through the choice of a suitable data acquisition protocol.

The relation between Φ and the exitance $\Gamma(\xi, t)$ through the boundary $\partial\Omega$ is given by Fick's law,

$$\Gamma(\xi, t) = -c\kappa(\xi) \nabla_n \Phi(\xi, t). \quad (2)$$

If the source term q_0 in Eq. (1) is highly localized in time and space (an ultrashort pulse of light incident upon one point of the tissue surface), Γ approximates the exitance Green's function of the system. In analogy with the spatial case this is often referred to as the temporal point-spread function (TPSF).²⁰

The shape of the TPSF for any given source and detector position depends on the distribution of optical properties within the tissue and on the tissue geometry. In temporal optical imaging applications one seeks to reconstruct an image of the absorption and the scattering distribution from a set of TPSF measurements at different source and detector positions. For improving the efficiency of the reconstruction process, it is desirable to express the information contained in a TPSF by a small number of statistical measures. Previously,¹⁴ we discussed the use of the time-integrated exitance E and the

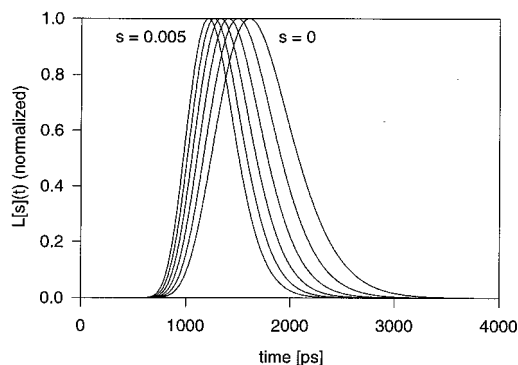


Fig. 1. Effect of exponential filtering of TPSF, showing normalized exponentially weighted TPSF calculated for the measurement across a homogeneous circle with a radius of 25 mm, $\mu_a = 0.025 \text{ mm}^{-1}$, and $\mu_s' = 2.0 \text{ mm}^{-1}$. s ranged between 0 and 0.005 ps^{-1} in steps of 0.001 ps^{-1} .

moments $\langle t^n \rangle$ of the temporal distribution, which are given in terms of the Mellin transform m of $\Gamma(t)$,

$$m[\Gamma(t), k] \equiv \int_0^\infty t^{k-1} \Gamma(t) dt, \quad (3)$$

as

$$E = m[\Gamma, 1], \quad (4)$$

$$\langle t^n \rangle = \frac{m[\Gamma, n+1]}{m[\Gamma, 1]}, \quad n = 1, 2, \dots \quad (5)$$

We propose the Laplace transform (L) of Γ as a further measure that can be added to the set of measurement types used to characterize the TPSF:

$$L[\Gamma(t), s] \equiv \int_0^\infty \exp(-st) \Gamma(t) dt, \quad (6)$$

where s is a free parameter governing the extent of the exponential attenuation of the temporal profile. The Laplace transform essentially weights the TPSF with an exponential filter, thereby suppressing the contribution of longer flight times. The effect of applying an exponential filter to the temporal response function is shown in Fig. 1 for values of s in the range between 0 and 0.005 ps^{-1} (inverse picoseconds). The curves were calculated numerically with the finite-element model as described below and with a finite-difference method for the temporal sampling. The effect of the exponential filter is to move the mean of the temporal distribution toward earlier times by increasing the weight of the early-arriving photons. The curves have been normalized owing to the large dynamic range for different values of s . The motivation for this approach is the well-known fact that the volume of tissue sampled by photons depends on their path length or flight time. Early-arriving photons will have deviated less from the direct line of sight between the source and detector than will late-arriving photons. Therefore it can be expected that by applying a temporal filter we can

vary the sampling region. In principle, it would also be possible to use a step function to filter the TPSF. This corresponds to the time-gating method proposed by Hebden *et al.*²¹ in an attempt to improve the spatial resolution of the reconstruction. The exponential filter has the advantage that it can be coded efficiently into the finite-element light transport model, as described in Section 3.

To avoid the problem of absolute intensity measurements that are difficult to obtain in practice, we normalize $L[\Gamma, s]$ with the integrated exitance,

$$\bar{L}[\Gamma, s] \equiv L[\Gamma, s]/E. \quad (7)$$

3. Finite-Element Calculations

A. Forward Problem

We use the finite-element method (FEM) to solve the diffusion equation [Eq. (1)] numerically for inhomogeneous and irregular object geometries. A detailed description of the application of FEM to the diffusion problem has been given previously^{22,23} and is not repeated here. Let domain Ω be discretized in P elements, joined at D nodal points. The discrete formulation of Eq. (1) is given by the matrix equation

$$[\mathbf{K}(\kappa) + \mathbf{C}(\mu_a)]\Phi(t) + \mathbf{B} \frac{\partial \Phi}{\partial t} = \mathbf{Q}(t), \quad (8)$$

where $\Phi, \mathbf{Q} \in \mathbb{R}^D$ are the solution and source vectors, respectively, sampled at the nodes and $\mathbf{K}, \mathbf{C}, \mathbf{B} \in [\mathbb{R}^D \times \mathbb{R}^D]$ are the system matrices that represent the terms for diffusion, absorption, and temporal variation, respectively. The piecewise linear approximation $\Phi^h(\mathbf{r}, t)$ to $\Phi(\mathbf{r}, t)$ is found by interpolation of nodal solutions with the use of linear basis functions u :

$$\Phi^h(\mathbf{r}, t) = \sum_{i=1 \dots D} \Phi_i(t) u_i(\mathbf{r}). \quad (9)$$

We presented previously²² a finite-difference scheme to sample $\Phi(t)$ at discrete time steps t_n . This could, in principle, be used for calculating the Laplace transform explicitly. This method, however, is not efficient because for reasons of numerical stability and accuracy the temporal step size must be of the order of $O(10^{-3})$ with respect to the total required temporal range.

By deriving a direct expression for the Laplace transform, we can avoid the explicit temporal sampling completely. If we use the fact that

$$L \left[\frac{\partial \Phi}{\partial t}, s \right] = s \cdot L[\Phi, s], \quad (10)$$

the Laplace transform of Eq. (8) becomes

$$\int_0^\infty \exp(-st) (\mathbf{K} + \mathbf{C} + s\mathbf{B}) \Phi(t) dt = \int_0^\infty \exp(-st) \mathbf{Q}(t) dt, \quad (11)$$

or

$$(\mathbf{K} + \mathbf{C} + s\mathbf{B}) L[\Phi(t), s] = L[\mathbf{Q}(t), s]. \quad (12)$$

If \mathbf{Q} is a δ function in time, $\mathbf{Q}(\mathbf{r}, t) = \delta(t - t_0) \mathbf{Q}_0(\mathbf{r})$, then $L[\mathbf{Q}(\mathbf{r}, t), s] = \mathbf{Q}_0(\mathbf{r})$, and therefore

$$L[\Phi(t), s] = (\mathbf{K} + \mathbf{C} + s\mathbf{B})^{-1} \mathbf{Q}_0. \quad (13)$$

With Eq. (2) we get an expression for the Laplace transform of the measurement Γ ,

$$L[\Gamma(t), s] = -c\kappa \nabla_n L[\Phi(t), s]. \quad (14)$$

Note that in Eq. (13) the structure of the system matrices \mathbf{C} and $s\mathbf{B}$ is identical if s/c is regarded as a uniform absorption coefficient; i.e., $s\mathbf{B} = \mathbf{C}(s/c)$.¹¹ Physically the application of a Laplace transform to the temporal profile is therefore equivalent to a uniform absorption increase by $\bar{\mu}_a = s/c$.

B. Jacobian and Photon Measurement Density Functions

Consider S source positions $\zeta_i \in \partial\Omega$, ($i = 1 \dots S$) and N measurement positions $\xi_j \in \partial\Omega$, ($j = 1 \dots N$). Let $\mathbf{M} = \{M_i\}$, $i = 1 \dots S \cdot N$ be the set of boundary measurements from all combinations of ζ and ξ , and let $\mathbf{p} = \{p_j\}$, ($j = 1 \dots P$) be the vector of absorption or scattering parameters, discretized on the FEM mesh. Image reconstruction algorithms based on multidimensional error minimization algorithms generally require the computation of the Jacobian matrix

$$\mathbf{J}[p] = \{J_{ij}[p]\} = \{\partial M_i / \partial p_j\}. \quad (15)$$

A straightforward way to obtain \mathbf{J} is by explicitly perturbing each element in succession by a sufficiently small amount and then calculating the measurement perturbation with the forward model. However, this is computationally inefficient as it requires a separate forward calculation for each source and each of the P elements.

Previously we described a reciprocity principle to obtain expressions for \mathbf{J} for a variety of measurement types that can be computed efficiently by the FEM model.^{24,25} In direct analogy with the expressions for the Jacobian in the Fourier domain given in Refs. 24 and 25 we can form the pointwise continuous Jacobian $\mathbf{J}(\mathbf{r})$ (italics are used to distinguish from the discrete Jacobian matrix) for the unnormalized Laplace transform, for both absorption perturbations α and diffusion perturbations v :

$$\begin{aligned} J_\alpha^{L[s]}(\xi_j, \zeta_i, s, \mathbf{r}) &= \sum_{k, l | N_k, N_l \in \tau(\mathbf{r})} L[\Phi_k^{(i)}, s] \\ &\quad \times L[\Phi_{\text{Adj}, l}^{(j)}, s] u_k(\mathbf{r}) u_l(\mathbf{r}), \end{aligned} \quad (16)$$

$$\begin{aligned} J_v^{L[s]}(\xi_j, \zeta_i, s, \mathbf{r}) &= \sum_{k, l | N_k, N_l \in \tau(\mathbf{r})} L[\Phi_k^{(i)}, s] \\ &\quad \times L[\Phi_{\text{Adj}, l}^{(j)}, s] \nabla u_k(\mathbf{r}) \cdot \nabla u_l(\mathbf{r}), \end{aligned} \quad (17)$$

where $\Phi^{(i)}$ and $\Phi_{\text{Adj}}^{(j)}$ are the nodal forward solutions calculated for direct source i at ζ_i and adjoint source j at ξ_j . u_i is the linear basis function associated with

node i . $\tau(\mathbf{r})$ is the element containing \mathbf{r} , and the summations are performed over the nodes of $\tau(\mathbf{r})$. A detailed discussion of the determination of the adjoint source vector required to calculate Φ_{Adj} is given in Ref. 25.

To obtain the Jacobian matrix for the element basis, we must integrate J over each element τ_j :

$$\mathbf{J}_\alpha^{(L[s])} = \{J_{ij,\alpha}^{(L[s])}(\xi_l, \zeta_k, s, \tau_j)\} = \left\{ \int_{\tau_j} \mathcal{J}_\alpha^{(L[s])}(\xi_l, \zeta_k, s, \mathbf{r}) d\mathbf{r} \right\}, \quad (18)$$

$$\mathbf{J}_v^{(L[s])} = \{J_{ij,v}^{(L[s])}(\xi_l, \zeta_k, s, \tau_j)\} = \left\{ \int_{\tau_j} \mathcal{J}_v^{(L[s])}(\xi_l, \zeta_k, s, \mathbf{r}) d\mathbf{r} \right\}. \quad (19)$$

Index i denotes the absolute measurement number. The Jacobian for the normalized Laplace transform $\bar{L} = L/E$ is given by the quotient rule:

$$\mathbf{J}_\alpha^{(\bar{L}[s])} = \frac{\mathbf{J}_\alpha^{(L[s])}}{E} - \frac{\mathbf{J}_\alpha^{(E)} L[s]}{E^2} = \frac{\mathbf{J}_\alpha^{(L[s])}}{E} - \bar{L}[s] \mathbf{J}_\alpha^{(\log E)}, \quad (20)$$

$$\mathbf{J}_v^{(\bar{L}[s])} = \frac{\mathbf{J}_v^{(L[s])}}{E} - \frac{\mathbf{J}_v^{(E)} L[s]}{E^2} = \frac{\mathbf{J}_v^{(L[s])}}{E} - \bar{L}[s] \mathbf{J}_v^{(\log E)}. \quad (21)$$

It is instructive to look at individual rows of \mathbf{J} because these provide a spatial map of the sensitivity of a particular measurement to a parameter perturbation. We denote these maps as photon measurement density functions (PMDF). Examples of PMDF for Laplace data are given in Section 4.

4. Results and Discussion

A. Forward Data

To validate the direct method for calculating the Laplace transform with FEM, we compare data obtained by the direct method with data from explicit sampling in time with a finite-difference method. For the latter, 1000 time steps at an interval of 5 ps were used. Figure 2 (top) shows $L[s](\theta)$ on the boundary of a homogeneous circle obtained by two-dimensional forward calculation (radius 25 mm, $\mu_a = 0.025 \text{ mm}^{-1}$, $\mu_s' = 2 \text{ mm}^{-1}$), where θ is the angle between the source and measurement sites, measured at the center of the circle. The FEM mesh consisted of 3691 nodes and 7200 elements. On a Sun SPARC 20 workstation the computation time for the direct method was 11 s, while the finite difference sampling required 435 s. This clearly demonstrates the advantage of the direct method. The performance gain is consistent with the timings reported for the calculation of the first moment in Ref. 14 although the absolute times are lower here as a result of the use of a faster computer. Figure 2 (middle) shows \bar{L} for the same cases, and Fig. 2 (bottom) shows the relative error between directly and explicitly generated data for both cases. The agreement is best for small values of s , but even at $s = 0.01 \text{ ps}^{-1}$ the

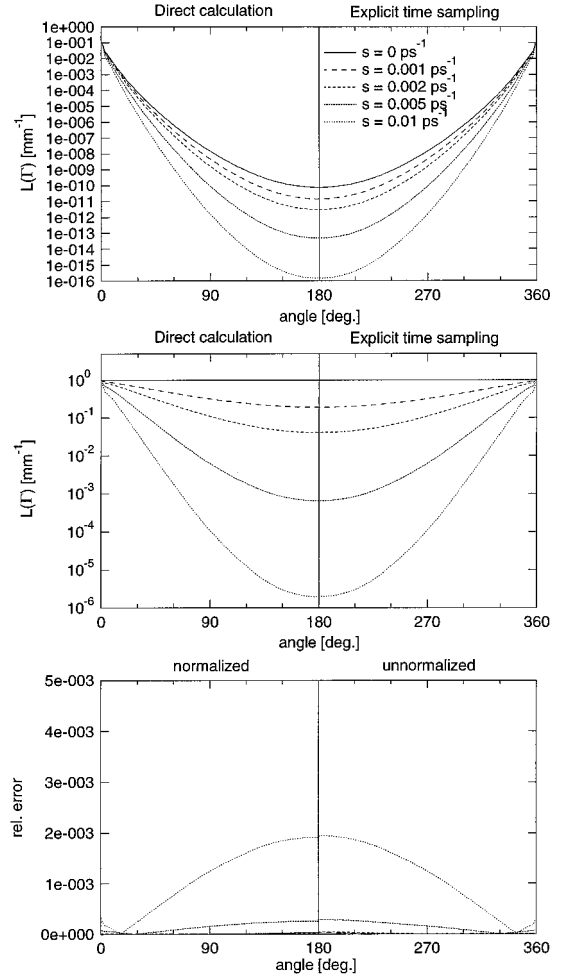


Fig. 2. Comparison of Laplace transforms on the boundary of a homogeneous circle obtained by the direct method and by explicit finite-difference time sampling. Values are plotted as function of angular source–detector spacing: (top) Unnormalized, (middle) normalized, (bottom) relative errors for both cases.

relative error is less than 0.2%. If required, we can improve the accuracy at high values of s by increasing the FEM mesh resolution.

B. Photon Measurement Density Functions

The calculation of PMDF, apart from their use in forming the Jacobian, is instructive in its own right by allowing one to visualize the regions of sensitivity of a measurement that directly affect the obtainable image resolution. In the following PMDF calculations we use the same homogeneous circular object as in Section 4.A. Source and detector are placed on opposite sides. Figure 3 compares absorption PMDF for the normalized Laplace transform ($\mathbf{J}_\alpha^{(\bar{L}[s])}$) for different values of s on a linear scale. Note that it was necessary to scale all plots individually because of the large dynamic variation between PMDF of different s . From top to bottom, $s = 0.001, 0.01, 0.1 \text{ ps}^{-1}$. Figure 4 shows $\mathbf{J}_v^{(L[s])}$ for the same cases. Because of the strong maxima of \mathbf{J}_v , close to the source

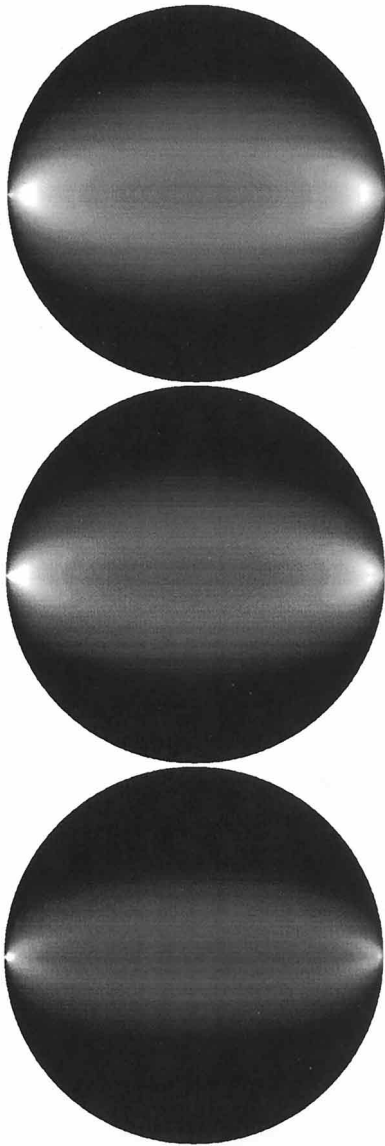


Fig. 3. Absorption PMDF $J_{\alpha}^{L[s]}$ for $s = 0.001 \text{ ps}^{-1}$ (top), 0.01 ps^{-1} (middle), and 0.1 ps^{-1} (bottom). Object is homogeneous circle (radius 25 mm) with $\mu_{\alpha} = 0.025 \text{ mm}^{-1}$ and $\mu_{s'} = 2 \text{ mm}^{-1}$. Images are scaled individually.

and the detector positions these PMDF are displayed on a logarithmic scale.

For \mathbf{J}_{α} we find that by increasing the value of s the PMDF can be tightened to some degree around the direct line of sight between source and detector. This is expected as the exponential weighting of the TPSF suppresses predominantly the late-arriving photons that have deviated furthest from the straight path between source and detector. To quantify this effect, the normalized cross sections of the images in Fig. 3 along the vertical radial are plotted in Fig. 5 (top), together with the FWHM of the cross sections (bottom). Note the characteristic shape of the PMDF, which is positive overall but has a local minimum along the central axis between source and detector. A similar behavior has been observed for the

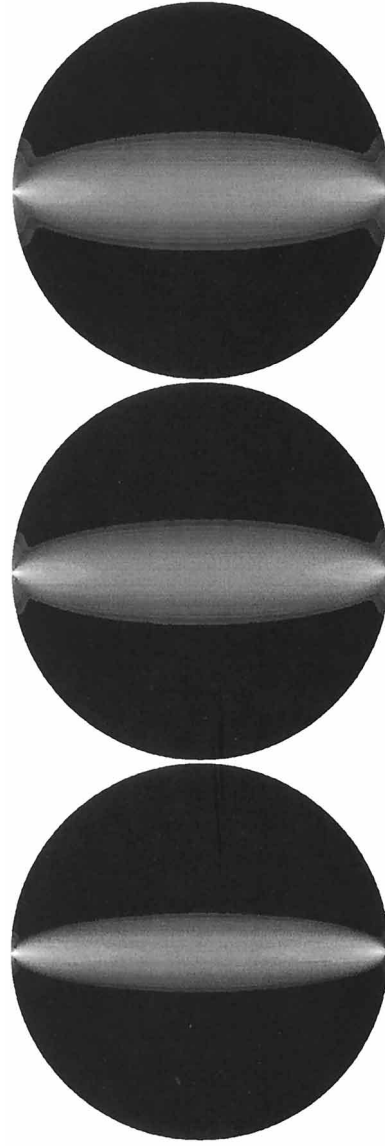


Fig. 4. Diffusion PMDF $J_{\nu}^{L[s]}$ for the same values of s as in Fig. 3. Images are logarithmic and scaled individually.

PMDF of temporal moments.²⁵ Qualitatively this feature of \mathbf{J}_{α} may be explained as follows: An absorption perturbation far away from the direct line of sight from source to detector affects predominantly multiply scattered, late-arriving photons, i.e., the tail of the temporal signal profile. This reduces the denominator of Eq. (7) but has little effect on the numerator, thereby producing the positive lobes of the PMDF. As the perturbation moves toward the axis, it starts to affect the earlier part of the temporal profile and thus reduces the numerator of Eq. (7), causing the observed local minimum.

For \mathbf{J}_{ν} , we find that the PMDF cross sections are narrower than for the absorption case (Fig. 6), which would suggest that a higher resolution can be achieved in reconstructions of κ than in those of μ_{α} . However, Fig. 4 shows that \mathbf{J}_{ν} exhibits strong maxima close to the surface below the source and detector

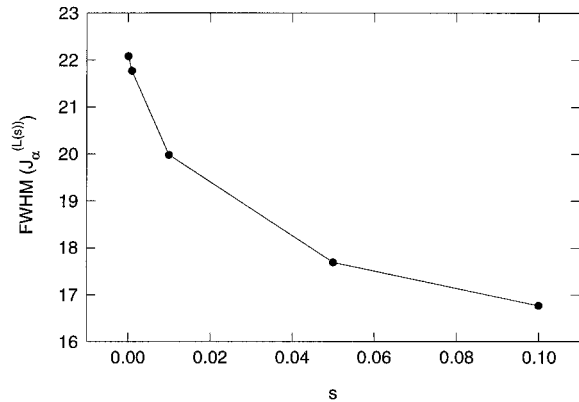
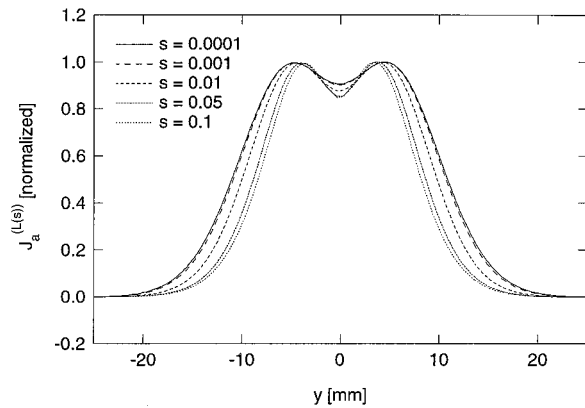


Fig. 5. (top) Normalized cross sections of images in Fig. 3 along the vertical radial. (bottom) FWHM as a function of s .

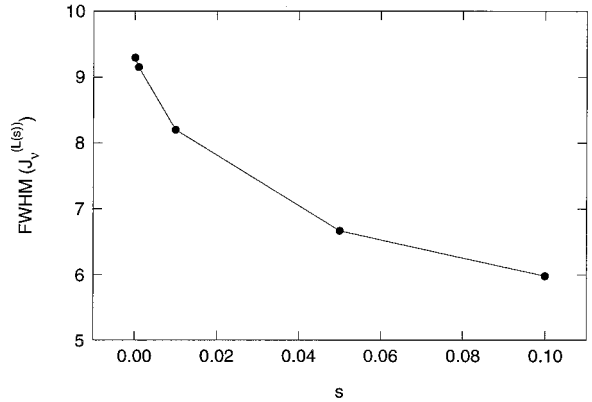
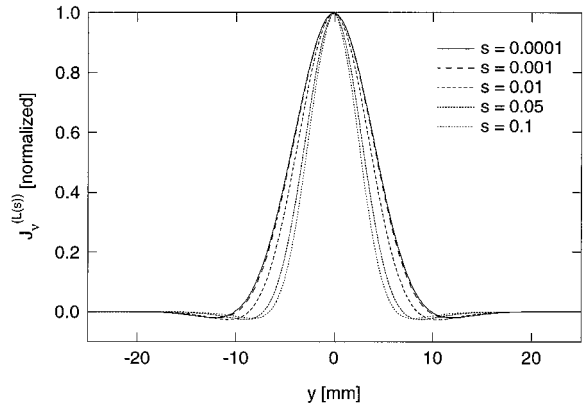


Fig. 6. (top) Normalized cross sections of images in Fig. 4 for the scatter case. (bottom) FWHM as a function of s .

positions, while the sensitivity in the central region is strongly reduced compared with \mathbf{J}_α . This difference in the behavior of absorption and scattering PMDF has been observed previously for other measurement types.²⁵ It indicates that, despite the narrower cross sections, the resolution of κ images in the interior of large objects will be much lower than the resolution of μ_α images.

C. Test Reconstruction

It has been known for several years that the simultaneous reconstruction of absorption and scattering images requires the use of multiple measurement types to disambiguate the two maps.^{26,27} To demonstrate the benefit of including the Laplace transform in the simultaneous reconstruction of absorption and scattering maps, we present images reconstructed from simulated data by using different combinations of data types. The object is a circle with a radius of 25 mm with homogeneous background [$\mu_\alpha(h) = 0.025 \text{ mm}^{-1}$, $\mu_s'(h) = 2 \text{ mm}^{-1}$] and three embedded perturbations, 1, 2, and 3, with parameters $\mu_\alpha[1] = 2\mu_\alpha[h]$, $\mu_s'[1] = \mu_s'[h]$, $\mu_\alpha[2] = \mu_\alpha[h]$, $\mu_s'[2] = 2\mu_s'[h]$, $\mu_\alpha[3] = 2\mu_\alpha[h]$, $\mu_s'[3] = 2\mu_s'[h]$. The FEM mesh contained 1441 nodes and 2700 triangular elements. Data were generated for all 256 combinations of 16 source and 16 measurement positions, equally spaced along the boundary. We added noise to the data by

assuming that 10^5 photons were collected at each measurement position and by using a model of photon statistics described previously.²⁸ Figure 7(a) shows the targets for the absorption (left) and the scattering images (right). Figures 7(b), 7(c), and 7(d) are reconstructions from $\langle t \rangle$, from $\langle t \rangle$ and $\langle t^2 \rangle$, and from $\langle t \rangle$ and $\bar{L}[0.01]$, respectively. The gray-scale range for the μ_α and μ_s' reconstructions is shown at the bottom. Reconstructions were carried out by a standard iterative scheme reported previously.^{11,15,24,25} A public-domain version of the reconstruction software is available on the internet.²⁹ It can be seen that the combination of temporal moment and Laplace transforms achieves the best result of the investigated cases, in particular with respect to the absorption image.

5. Conclusion

We present the mathematical framework to implement the normalized Laplace transform as a measurement type in time-resolved optical tomography. This includes both a computationally efficient forward model for direct calculation of data without the need for explicit time sampling and an efficient method for generating the Jacobian by use of the reciprocity principle. Use of the Laplace transform has a twofold advantage: Physically, it is related to time-gating techniques, which aim to increase image

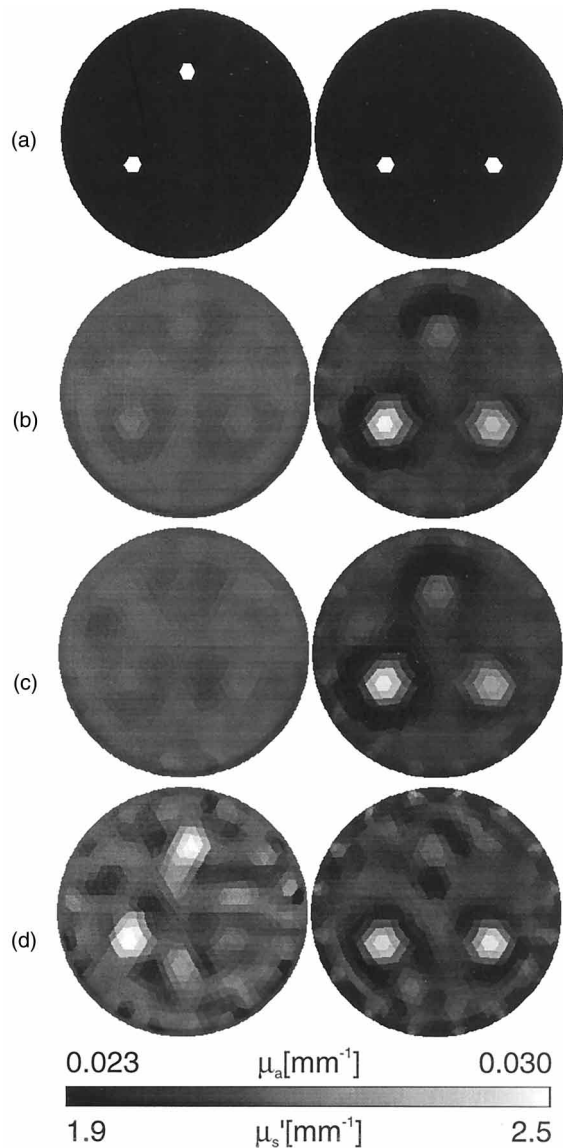


Fig. 7. Simultaneous reconstruction of μ_a and μ_s' of a test object with embedded absorbing and scattering inhomogeneities: (a) target, (b) reconstruction from $\langle t \rangle$ only, (c) reconstructions from $\langle t \rangle$ and $\langle t^2 \rangle$, and (d) reconstructions from $\langle t \rangle$ and $L(s = 0.01)$; (left) μ_a , (right) μ_s' .

resolution with the use of only early light in the imaging process. This can be readily seen in our finding that the width of the PMDF decreases when the Laplace parameter s is increased. In practice, the choice of s will be limited by the decrease in signal-to-noise ratio resulting from the poor statistics of the early part of the temporal response signal.

From a purely theoretical point of view the Laplace transform offers a measurement type complementary to the temporal moments. The choices of measurement types for time-of-flight systems have so far been multiple temporal moments or a moment and the time-integrated exitance. However, multiple moments are strongly correlated,¹⁵ and the use of intensity data should be avoided where possible as it

requires calibration and scaling procedures, such as the calibration against a homogeneous sample, which are often not available in real-life applications.

This work was made possible by funding from Action Research.

References

1. J. C. Hebden and R. A. Kruger, "Transillumination imaging performance: a time of flight imaging system," *Med. Phys.* **17**, 351–356 (1990).
2. A. D. Edwards, J. S. Wyatt, C. E. Richardson, D. T. Delpy, M. Cope, and E. O. R. Reynolds, "Cotside measurement of cerebral blood flow in ill newborn infants by near infrared spectroscopy," *Lancet* **2**, 770–771 (1988).
3. J. S. Wyatt, M. Cope, D. T. Delpy, C. E. Richardson, A. D. Edwards, S. C. Wray, and E. O. R. Reynolds, "Quantitation of cerebral blood volume in newborn infants by near infrared spectroscopy," *J. Appl. Physiol.* **68**, 1086–1091 (1990).
4. M. Tamura, "Multichannel near-infrared optical imaging of human brain activity," in *Advances in Optical Imaging and Photon Migration*, R. R. Alfano and J. G. Fujimoto, eds., Vol. 2 of OSA Trends in Optics and Photonics Series (Optical Society of America, Washington, D.C., 1996), pp. 8–10.
5. R. A. de Blasi, M. Cope, C. E. Elwell, F. Safoue, and M. Ferrari, "Noninvasive measurement of human forearm oxygen consumption by near-infrared spectroscopy," *J. Appl. Physiol.* **67**, 20–25 (1993).
6. H. Jiang, K. D. Paulsen, and U. L. Osterberg, "Optical image reconstruction using dc data: simulations and experiments," *Phys. Med. Biol.* **41**, 1483–1498 (1996).
7. H. Jiang, K. D. Paulsen, and U. L. Osterberg, "Optical image reconstruction using frequency-domain data: simulations and experiments," *J. Opt. Soc. Am. A* **13**, 253–266 (1995).
8. K. D. Paulsen and H. Jiang, "Enhanced frequency-domain optical image reconstruction in tissues through total variation minimization," *Appl. Opt.* **35**, 3447–3458 (1996).
9. M. S. Patterson, B. W. Pogue, and B. C. Wilson, "Computer simulation and experimental studies of optical imaging with photon density waves," in *Medical Optical Tomography: Functional Imaging and Monitoring*, G. Muller, B. Chance, R. Alfano, S. Arridge, J. Beuthan, E. Gratton, M. Kaschke, B. Masters, S. Svanberg, and P. van der Zee, eds., (Society of Photo-Optical Instrumentation Engineers, Bellingham, Wash., 1993), pp. 513–533.
10. A. J. Joblin, "Method of calculating the image resolution of a near infrared time-of-flight tissue-imaging system," *Appl. Opt.* **35**, 752–757 (1996).
11. M. Schweiger, S. R. Arridge, and D. T. Delpy, "Application of the finite-element method for the forward and inverse models in optical tomography," *J. Math. Imag. Vision* **3**, 263–283 (1993).
12. S. R. Arridge and M. Schweiger, "Reconstruction in optical tomography using MRI-based prior knowledge," in *Information Processing in Medical Imaging '95*, Y. Bizais, C. Barillot, and R. di Paola, eds., (Springer-Verlag, Berlin, 1995), pp. 77–88.
13. M. Schweiger and S. R. Arridge, "Optimal data types in optical tomography," in *Lecture Notes in Computer Science, Vol. 1230*, J. Duncan and G. Gindi, eds. (Springer-Verlag, Berlin, 1997), pp. 71–84.
14. S. R. Arridge and M. Schweiger, "Direct calculation of the moments of the distribution of photon time of flight in tissue with a finite-element method," *Appl. Opt.* **34**, 2683–2687 (1995).
15. S. R. Arridge and M. Schweiger, "The use of multiple data types in time-resolved optical absorption and scattering to-

- mography (TOAST),” in *Mathematical Methods in Medical Imaging II*, J. N. Wilson and D. C. Wilson, eds., Proc. SPIE **2035**, 218–229 (1993).
16. B. W. Pogue and M. S. Patterson, “Frequency-domain optical absorption spectroscopy of finite tissue volumes using diffusion theory,” *Phys. Med. Biol.* **39**, 1157–1180 (1994).
 17. J. L. Karagiannes, Z. Zhang, B. Grossweiner, and L. I. Grossweiner, “Applications of the 1-D diffusion approximation to the optics of tissues and tissue phantoms,” *Appl. Opt.* **28**, 2311–2317 (1989).
 18. M. Keijzer, W. M. Star, and P. R. M. Storchi, “Optical diffusion in layered media,” *Appl. Opt.* **27**, 1820–1824 (1988).
 19. J. C. Haselgrove, J. C. Schotland, and J. S. Leigh, “Long-time behavior of photon diffusion in an absorbing medium: application to time-resolved spectroscopy,” *Appl. Opt.* **31**, 2678–2683 (1992).
 20. D. T. Delpy, M. Cope, P. van der Zee, S. R. Arridge, S. Wray, and J. Wyatt, “Estimation of optical pathlength through tissue from direct time of flight measurement,” *Phys. Med. Biol.* **33**, 1433–1442 (1988).
 21. J. C. Hebden, R. A. Kruger, and K. S. Wong, “Time-resolved imaging through a highly scattering medium,” *Appl. Opt.* **30**, 788–794 (1991).
 22. S. R. Arridge, M. Schweiger, M. Hiraoka, and D. T. Delpy, “A finite element approach for modeling photon transport in tissue,” *Med. Phys.* **20**, 299–309 (1993).
 23. M. Schweiger, S. R. Arridge, M. Hiraoka, and D. T. Delpy, “The finite element model for the propagation of light in scattering media: boundary and source conditions,” *Med. Phys.* **22**, 1779–1792 (1995).
 24. S. R. Arridge, “Photon measurement density functions. Part 1: Analytical forms,” *Appl. Opt.* **34**, 7395–7409 (1995).
 25. S. R. Arridge and M. Schweiger, “Photon measurement density functions. Part 2: Finite element calculations,” *Appl. Opt.* **34**, 8026–8037 (1995).
 26. S. R. Arridge, M. Schweiger, and D. T. Delpy, “Iterative reconstruction of near infra-red absorption images,” in *Inverse Problems in Scattering and Imaging*, M. A. Fiddy, ed., Proc. SPIE **1767**, 372–383 (1992).
 27. S. R. Arridge, M. Schweiger, M. Hiraoka, and D. T. Delpy, “Performance of an iterative reconstruction algorithm for near-infrared absorption and scatter imaging,” in *Photon Migration and Imaging in Random Media and Tissues*, B. Chance and R. R. Alfano, eds., Proc. SPIE **1888**, 360–371 (1993).
 28. S. R. Arridge, M. Hiraoka, and M. Schweiger, “Statistical basis for the determination of optical pathlength in tissue,” *Phys. Med. Biol.* **40**, 1539–1558 (1995).
 29. TOAST reconstruction package available at <http://www.med-physics.ucl.ac.uk/toast/index.htm>.